LETTER

doi:10.1038/nature16173

Nanoscale intimacy in bifunctional catalysts for selective conversion of hydrocarbons

Jovana Zečević[1], Gina Vanbutsele[2], Krijn P. de Jong[1] & Johan A. Martens[2]

The ability to control nanoscale features precisely is increasingly being exploited to develop and improve monofunctional catalysts[1–4]. Striking effects might also be expected in the case of bifunctional catalysts, which are important in the hydrocracking of fossil and renewable hydrocarbon sources to provide high-quality diesel fuel[5–7]. Such bifunctional hydrocracking catalysts contain metal sites and acid sites, and for more than 50 years the so-called intimacy criterion[8] has dictated the maximum distance between the two types of site, beyond which catalytic activity decreases. A lack of synthesis and material-characterization methods with nanometre precision has long prevented in-depth exploration of the intimacy criterion, which has often been interpreted simply as 'the closer the better' for positioning metal and acid sites[8–11]. Here we show for a bifunctional catalyst—comprising an intimate mixture of zeolite Y and alumina binder, and with platinum metal controllably deposited on either the zeolite or the binder—that closest proximity between metal and zeolite acid sites can be detrimental. Specifically, the selectivity when cracking large hydrocarbon feedstock molecules for high-quality diesel production is optimized with the catalyst that contains platinum on the binder, that is, with a nanoscale rather than closest intimacy of the metal and acid sites. Thus, cracking of the large and complex hydrocarbon molecules that are typically derived from alternative sources, such as gas-to-liquid technology, vegetable oil or algal oil[6,7], should benefit especially from bifunctional catalysts that avoid locating platinum on the zeolite (the traditionally assumed optimal location). More generally, we anticipate that the ability demonstrated here to spatially organize different active sites at the nanoscale will benefit the further development and optimization of the emerging generation of multifunctional catalysts[12–15].

Bifunctional catalysts for the conversion of hydrocarbons contain metal sites next to acid sites. In the case of the conversion of normal alkanes, the metal sites catalyse (de)hydrogenation reactions; the acid sites catalyse isomerization and cracking reactions, to obtain iso-alkanes of the same or reduced molecular weight, respectively[16]. The critical properties of these catalysts are the ratio of metal sites relative to acid sites, and the proximity of both sites to each other[8,17]. This latter aspect is further illustrated by the schematic presentation of hydrocracking reactions in Fig. 1. The normal alkene reaction intermediate has to diffuse from the metal site to the acid site; the iso-alkene reaction intermediate must diffuse the other way. If the distances are too large and diffusivity too low, concentration gradients develop and catalytic activity decreases. The intimacy criterion put forward by Weisz[8] in 1962 provides the maximum distance between both types of site, beyond which catalytic activity decreases. Since then it has been realized that, even more importantly, selectivity might also be affected by intimacy[9–11,18]: if the distances between metal and acid sites are large, iso-alkenes might undergo secondary reactions, giving rise to gas and to coke. Systematic quantitative studies on intimacy effects have been carried out only at the macroscale[8,11,18] (tens of micrometres and larger); meanwhile, in many other studies the metal function has been put as close as possible to the acid sites[6,9,19] (in particular in the case of metal dispersed in acid zeolite). These findings have led to the general belief that, as far as the intimacy of bifunctional catalysts goes, 'the closer the better'.

Here we report a new methodology for controlling and imaging the intimacy of metal and acid sites at the nanoscale, with large positive effects on selectivity. Our strategy for controlling the distance between metal and acid sites starts with an intimate mixture of 50 wt% mesoporous zeolite Y (designated Y; this provides the acid sites) and 50 wt% γ-alumina binder (designated as A), obtained by extrusion and referred to as Y/A. Energy dispersive X-ray (EDX) spectroscopy maps of a 70-nm-thick ultramicrotomed slice of Y/A (Fig. 2) show the two components mixed at the nanoscale, with zeolite crystals (of diameter 500–1,000 nm) being surrounded by at least one layer of alumina, and alumina regions not exceeding 5 μm in length. Porosity, apparent as black voids in the EDX map (Fig. 2a) and as revealed by nitrogen physisorption (Extended Data Fig. 1), enables molecular transport via diffusion throughout the extrudates.

We then exploit the difference between ion exchange and electrostatic adsorption[20,21] to direct the subsequent deposition of platinum (Pt) metal precursor: ion exchange at pH5 with an aqueous solution of $Pt(NH_3)_4(NO_3)_2$ results in Pt cations being located exclusively on the zeolite component, whereas electrostatic adsorption at pH3 from

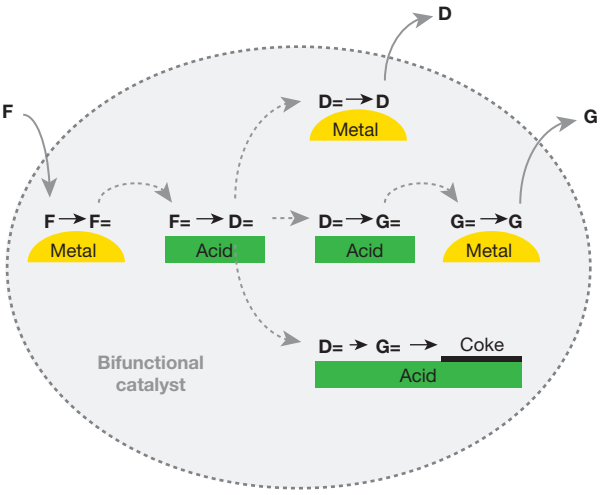

Figure 1 | Scheme of hydrocracking reactions that use a bifunctional catalyst. Feed normal alkane molecules (F) are dehydrogenated on a metal surface, producing alkene intermediates (F=). The alkenes diffuse to zeolite Brønsted acid sites, on which they undergo acid-catalysed skeletal isomerization, which can be followed by one (D=) or more (G=) cracking events, sometimes leading to coke formation. Isomerized (D=) and/or cracked (D=, G=) alkene intermediates diffuse to the metal site and are hydrogenated to form isomerized or cracked products D (diesel) and G (gas).

[1]Inorganic Chemistry and Catalysis, Debye Institute for Nanomaterials Science, Utrecht University, Universiteitsweg 99, 3584 CG Utrecht, The Netherlands. [2]Centre for Surface Chemistry and Catalysis, KU Leuven, Celestijnenlaan 200F Postbus 2461, B-3001 Leuven, Belgium.

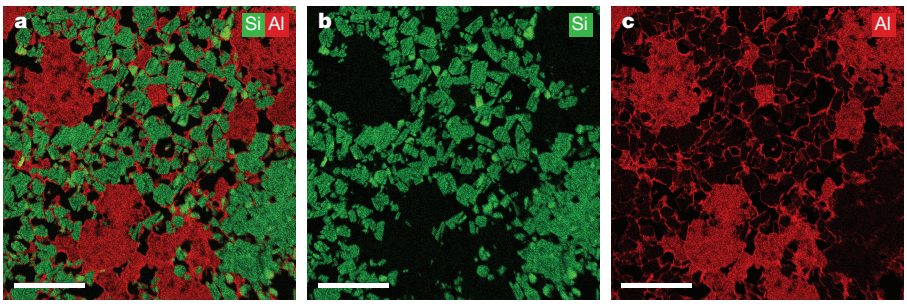

Figure 2 | Distribution of zeolite Y and alumina components within Y/A extrudates. a, EDX map of a 70-nm-thick section of a Y/A extrudate, showing the location of silicon (Si, green) and aluminium (Al, red), which are indicative of the presence of the zeolite Y and alumina components, respectively, of Y/A. **b**, EDX map showing only the Si (green) signal, corresponding to the presence of zeolite Y. **c**, EDX map showing only the Al (red) signal, most pronounced in regions containing pure alumina phase. Scale bars, 2 μm.

a solution of H_2PtCl_6 deposits Pt anions exclusively on the alumina component (see Methods). The resulting samples, Pt-Y/A and Pt-A/Y, are then either heat-treated in H_2, or heat-treated in H_2 followed by 1 vol% O_2 in N_2, respectively, to generate Pt metal particles with a size of about 3 nm (refs 22, 23). Inductively coupled plasma (ICP) analysis shows the Pt-Y/A and Pt-A/Y samples to have comparable Pt loading of 0.6 wt% and 0.7 wt%, respectively, which suffices to maintain the metal–acid balance needed for so-called ideal hydrocracking[11].

High-angle annular dark-field scanning transmission electron microscopy (HAADF-STEM) imaging and EDX elemental mapping of 70-nm-thick ultramicrotomed sections of Pt-Y/A (Fig. 3a, b and Extended Data Fig. 2a) confirms that Pt particles with a narrow size distribution, around 2.5 nm, are exclusively present in the zeolite crystals. Cutting the extrudates with ultramicrotomy to produce 70-nm-thick slices was crucial, to expose regions that contain purely the zeolite or alumina components. The images in Fig. 3a, b and electron tomography observations of Pt-Y/A (Extended Data Fig. 3a) reveal Pt nanoparticles located within the zeolite crystals even though they exceed the size of the micropores (roughly 1 nm), as reported previously[22]. In the Pt-A/Y sample, Pt particles with an average size of 3.5 nm and narrow size distribution reside exclusively on the alumina phase of the extrudates (Fig. 3c, d and Extended Data Fig. 2b). The absence of Pt particles in the zeolite crystals was confirmed by electron tomography (Extended Data Fig. 3b).

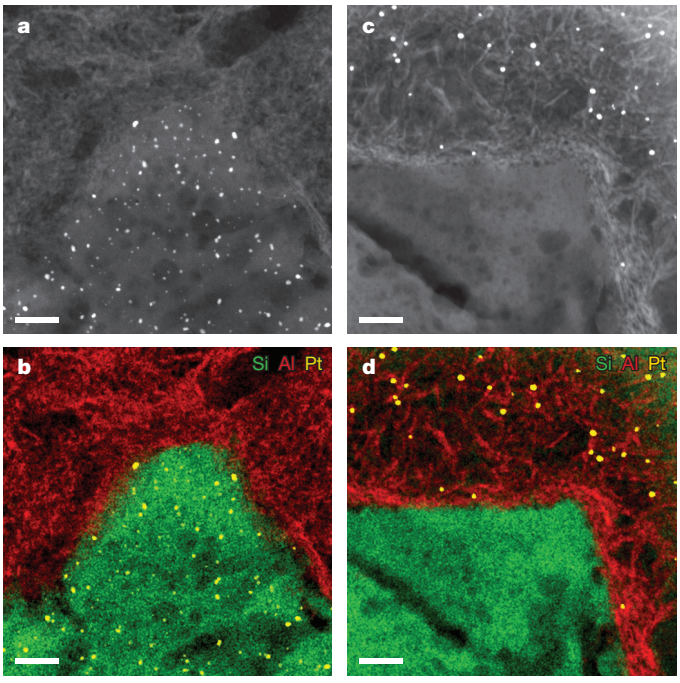

Figure 3 | Controlled deposition of platinum (Pt) on either the zeolite Y or the alumina component of Y/A extrudates. a, **b**, Pt-Y/A. The HAADF-STEM image (**a**) is of a 70-nm-thick section of a Pt-Y/A sample, with Pt particles of ~2.5 nm residing exclusively within the zeolite crystals, as evident from the EDX map (**b**) showing Pt (yellow), Si (green) and Al (red) signals. **c**, **d**, Pt-A/Y. Shown are an HAADF-STEM image (**c**) and EDX map (**d**) of a 70-nm-thick section of Pt-A/Y, with Pt particles (yellow) of ~3.5 nm residing exclusively on the alumina platelets (red) while the zeolite crystals (green) are empty. Scale bars, 50 nm.

The two catalysts thus have well defined structures, with Pt particles of comparable size located either inside the zeolite pores in closest proximity to the zeolite acid sites (in the Pt-Y/A sample), or within a nanoscale distance from the acid sites of the zeolite when located on the binder (in Pt-A/Y). Given that only about 0.6 wt% of Pt was loaded on the pre-shaped Y/A extrudates, no change in textural properties is expected compared with pristine Y/A extrudates. Temperature-programmed desorption of ammonia also indicates very similar acidities for the two catalysts (Extended Data Fig. 4). The two catalyst samples, with all structural parameters being identical except for the Pt location, therefore allow us to evaluate the impact of nanoscale intimacy on hydroconversion activity and selectivity.

The model feedstocks in our catalysis experiments are *n*-decane (*n*-C_{10}), *n*-nonadecane (*n*-C_{19}) and pristane (2,6,10,14-tetramethylpentadecane, *i*-C_{19}), with the two catalysts showing very similar *n*-C_{10} and *n*-C_{19} conversion activity (Fig. 4a, b). But Pt-Y/A, with its metal and zeolite acid sites in closest proximity, exhibits improved activity over Pt-A/Y in the conversion of multibranched *i*-C_{19} feed molecules (Fig. 4c). Assuming a typical, normal alkene diffusivity in zeolite Y of $1.0 \times 10^{-9}\,m^2\,s^{-1}$, the maximum intersite distance for *n*-alkane conversion has been estimated to be 4.5 μm, using the formula for the intimacy criterion[24]. With Pt on the alumina binder, the maximum distance between sites of about 500 nm is below this estimate and in line with the identical catalytic activities of the two catalysts for *n*-C_{10} and *n*-C_{19} conversion (Fig. 4a, b). For *i*-C_{19}, however, the lower activity of Pt-A/Y points to its activity being limited by transport of the bulky tetramethylbranched *i*-C_{19} alkene molecules, with their estimated diffusivity of only $1.0 \times 10^{-11}\,m^2\,s^{-1}$.

In contrast to their conversion activities, the selectivities of the two catalysts differ remarkably with all three feeds (Fig. 4d–f): the Pt-A/Y catalyst always produces a much higher yield of skeletal isomers, thus illustrating the importance of nanoscale intimacy between (de)hydrogenation and acid functions for the selectivity of bifunctional catalysts. Skeletal branching is succeeded by cracking of the carbon chains. Undesired multiple cracking leads to C_3–C_4 products[19], indicated as gas (Fig. 1). The cracking products formed at the same cracking conversion rate were identical for the two catalysts when the feedstock was *n*-C_{10}, but markedly different when the feedstock was *n*-C_{19} (Extended Data Fig. 5). In case of *n*-C_{19}, the product distribution was shifted towards the more desired range of middle distillates (C_{10}–C_{19}) when using the Pt-A/Y catalyst; the Pt-Y/A catalyst produced more gas (C_3–C_4) and naphtha (C_5–C_9) (Extended Data Fig. 5b).

High isomerization yield and limited secondary cracking are characteristics of ideal hydrocracking. In this regard, the Pt-A/Y catalyst, with

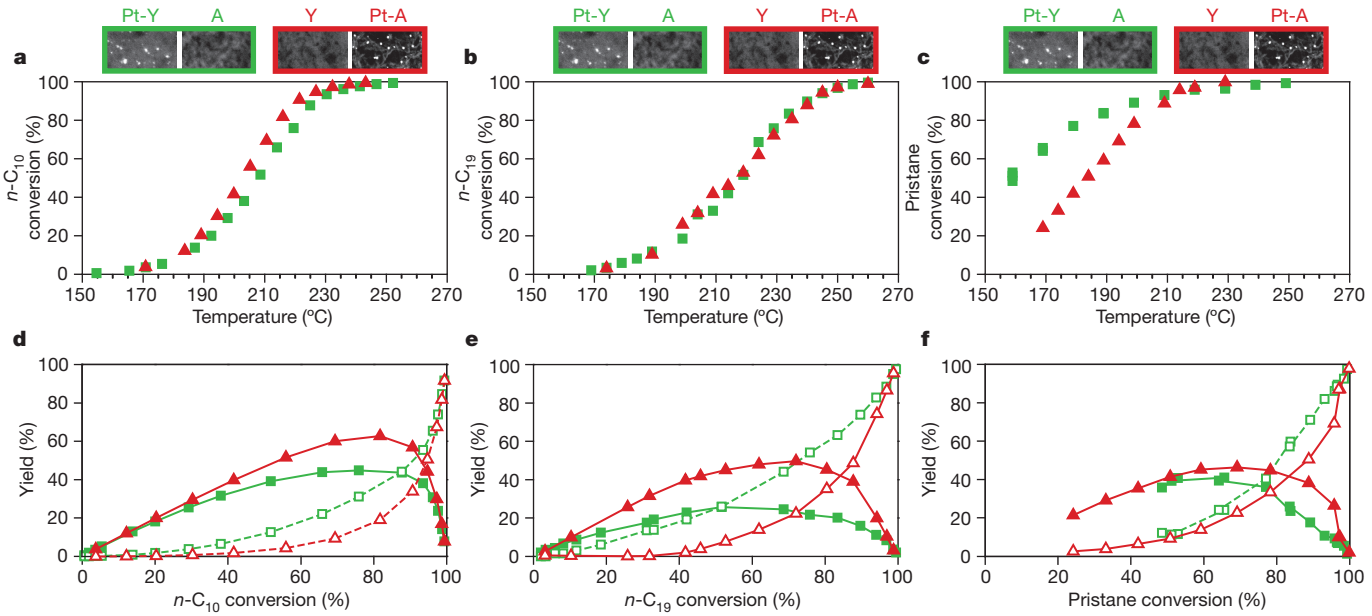

Figure 4 | Impact of nanoscale intimacy on hydrocracking activity and selectivity. a–c, The percentage of alkane feedstock converted is shown against the reaction temperature for Pt-Y/A (green squares) or Pt-A/Y (red triangles) catalysts. The feedstocks are: **a**, *n*-decane (n-C_{10}); **b**, *n*-nonadecane (n-C_{19}); and **c**, pristane (i-C_{19}). **d–f**, Product yields from **d**, *n*-decane, **e**, *n*-nonadecane, and **f**, pristane feedstocks, when using Pt-Y/A (green) or Pt-A/Y (red) catalysts. Solid lines and filled symbols show the yields of isomerized products; dashed lines and open symbols show cracked products. Experiments were performed at a pressure of 0.45 MPa and a H_2/hydrocarbon molar ratio of 214 (*n*-decane); or a pressure of 0.65 MPa and a H_2/hydrocarbon molar ratio of 14.6 (*n*-nonadecane and pristane).

the metal function residing on alumina and thus more distant from the zeolite acid sites, outperforms the Pt-Y/A catalyst, in which Pt nanoparticles are located inside the zeolite micropores and are thus in more intimate contact with the acid sites. These findings contradict previous suggestions that having the metal and acid functions as close as possible promotes immediate hydrogenation of alkene intermediates and prevents undesired consecutive reactions such as multiple cracking[11] (Fig. 1). We note that in the earlier work *n*-hexadecane was often used as the feedstock, whereas we used a range of hydrocarbons (n-C_{10}, n-C_{19}, i-C_{19}), allowing us to delineate the effects of intimacy on activity and selectivity. Moreover, in earlier studies a systematic variation in intimacy was achieved by mixing separately functionalized powders at the macroscale (tens of micrometres and more)[8,11,18], whereas we used synthesis and characterization methods that allow for direct control of intimacy at the nanoscale and for observation of the reported large impact.

When using the catalyst Pt-Y/A, where the Pt metal function resides inside the zeolite crystals and in the highest possible intimacy with acid sites, feed molecules have to diffuse through the micropores to reach the metal sites. Once alkene intermediates are formed on the metal, we envisage them remaining trapped in the zeolite micropores because of their strong adsorption on acid sites and concomitant slow diffusion and longer residence times. This increases the probability of secondary reactions, particularly multiple cracking. With the catalyst Pt-A/Y, in which metal nanoparticles are located outside the zeolite crystals on the more easily accessible alumina binder, alkene intermediates formed on the metal sites diffuse through wide pores to the zeolite, where they immediately undergo isomerization. We suggest that alkene intermediates react mainly in the outer zeolite layers near the crystal surface, from where they can rapidly diffuse back to the metal sites on the alumina. This mechanism has been proposed for medium-pore zeolites exhibiting so-called pore mouth catalysis[25], and is now extended to reactions of heavy alkanes on large-pore zeolite Y.

Hydrocracking catalysts that involve sulfided nickel molybdenum on alumina–zeolite, in which metal (sulfide) particles are mainly on the alumina binder[9,26], are widely used and probably already meet the requirement that the optimal location for the metal function of bifunctional catalysts is not in the micropores of the zeolite, as long perceived, but rather on the binder or on the surface/in the mesopores of the zeolite. But with the worldwide growing interest in alternative feedstocks, such as those based on gas-to-liquids[6] technology and on vegetable oil and algal oil[7], molecules of even larger complexity and size present new challenges to the process of hydroconversion for high-quality diesel production. Improving hydrocracking catalysts generally, and in such challenging applications, will undoubtedly benefit from full control over the size and location of the metal function in complex catalysts, complementing recent efforts that have focused on nanozeolites[10,27], hierarchical zeolites[28], metal particle size[29] and nanoscale characterization[30] to improve our understanding. Our control strategy—and the methodology used to achieve it—can be extended to other bifunctional catalysts[12–15], and provides the opportunity for tailoring catalyst properties in accordance with the specific requirements of the target process, beyond a simple 'the closer the better' notion of intimacy.

Online Content Methods, along with any additional Extended Data display items and Source Data, are available in the online version of the paper; references unique to these sections appear only in the online paper.

Received 6 April; accepted 19 October 2015.

1. Torres Galvis, H. M. *et al.* Supported iron nanoparticles as catalysts for sustainable production of lower olefins. *Science* **335,** 835–838 (2012).
2. Cui, C., Gan, L., Heggen, M., Rudi, S. & Strasser, P. Compositional segregation in shaped Pt alloy nanoparticles and their structural behaviour during electrocatalysis. *Nature Mater.* **12,** 765–771 (2013).
3. Prieto, G., Zečević, J., Friedrich, H., de Jong, K. P. & de Jongh, P. E. Towards stable catalysts by controlling collective properties of supported metal nanoparticles. *Nature Mater.* **12,** 34–39 (2013).
4. Luo, W. *et al.* High performing and stable supported nano-alloys for the catalytic hydrogenation of levulinic acid to γ-valerolactone. *Nature Commun.* **6,** 6540 (2015).
5. Weitkamp, J. Catalytic hydrocracking—mechanisms and versatility of the process. *ChemCatChem* **4,** 292–306 (2012).
6. Bouchy, C., Hastoy, G., Guillon, E. & Martens, J. A. Fischer-Tropsch waxes upgrading via hydrocracking and selective hydroisomerization. *Oil Gas Sci. Technol.* **64,** 91–112 (2009).
7. Tran, N. H. *et al.* Catalytic upgrading of biorefinery oil from micro-algae. *Fuel* **89,** 265–274 (2010).
8. Weisz, P. B. Polyfunctional heterogeneous catalysis. *Adv. Catal.* **13,** 137–190 (1962).

9. Francis, J. *et al.* Design of improved hydrocracking catalysts by increasing the proximity between acid and metallic sites. *Appl. Catal. A* **409–410,** 140–147 (2011).
10. Kim, J., Kim, W., Seo, Y., Kim, J.-C. & Ryoo, R. n-Heptane hydroisomerization over Pt/MFI zeolite nanosheets: effects of zeolite crystal thickness and platinum location. *J. Catal.* **301,** 187–197 (2013).
11. Batalha, N., Pinard, L., Bouchy, C., Guillon, E. & Guisnet, M. n-Hexadecane hydroisomerization over Pt-HBEA catalysts. Quantification and effect of the intimacy between metal and protonic sites. *J. Catal.* **307,** 122–131 (2013).
12. Huber, G. W., Chheda, J. N., Barrett, C. J. & Dumesic, J. A. Production of liquid alkanes by aqueous-phase processing of biomass-derived carbohydrates. *Science* **308,** 1446–1450 (2005).
13. Gao, J. *et al.* Identification of molybdenum oxide nanostructures on zeolites for natural gas conversion. *Science* **348,** 686–690 (2015).
14. Yamada, Y. *et al.* Nanocrystal bilayer for tandem catalysis. *Nature Chem.* **3,** 372–376 (2011).
15. Peng, X. *et al.* Impact of hydrogenolysis on the selectivity of the Fischer–Tropsch synthesis: diesel fuel production over mesoporous zeolite-Y-supported cobalt nanoparticles. *Angew. Chem. Int. Edn* **54,** 4553–4556 (2015).
16. Coonradt, H. L. & Garwood, W. E. Mechanism of hydrocracking. *Ind. Eng. Chem. Process Des. Dev.* **3,** 38–45 (1964).
17. Guisnet, M. "Ideal" bifunctional catalysis over Pt-acid zeolites. *Catal. Today* **218–219,** 123–134 (2013).
18. Zhang, A., Nakamura, I., Aimoto, K. & Fujimoto, K. Isomerization of n-pentane and other light hydrocarbons on hybrid catalyst. Effect of hydrogen spillover. *Ind. Eng. Chem. Res.* **34,** 1074–1080 (1995).
19. Martens, J. A., Jacobs, P. A. & Weitkamp, J. Attempts to rationalize the distribution of hydrocracked products. II. Relative rates of primary hydrocracking modes of long chain paraffins in open zeolites. *Appl. Catal.* **20,** 283–303 (1986).
20. Schreier, M., Teren, S., Belcher, L., Regalbuto, J. R. & Miller, J. T. The nature of 'overexchanged' copper and platinum on zeolites. *Nanotechnology* **16,** S582–S591 (2005).
21. Cho, H.-R. & Regalbuto, J. R. The rational synthesis of Pt-Pd bimetallic catalysts by electrostatic adsorption. *Catal. Today* **246,** 143–153 (2015).
22. Zečević, J., van der Eerden, A. M. J., Friedrich, H., de Jongh, P. E. & de Jong, K. P. Heterogeneities of the nanostructure of platinum/zeolite Y catalysts revealed by electron tomography. *ACS Nano* **7,** 3698–3705 (2013).
23. Boubnov, A. *et al.* Structure–activity relationships of Pt/Al_2O_3 catalysts for CO and NO oxidation at diesel exhaust conditions. *Appl. Catal. B* **126,** 315–325 (2012).
24. Martens, J. A. & Jacobs, P. A. Introduction to acid catalysis with zeolites in hydrocarbon reactions. *Stud. Surf. Sci. Catal.* **137,** 633–671 (2001).
25. Martens, J. A. *et al.* Selective isomerization of hydrocarbon chains on external surfaces of zeolite crystals. *Angew. Chem. Int. Edn* **34,** 2528–2530 (1995).
26. Landau, M. V. *et al.* Hydrocracking of heavy vacuum gas oil with a $Pt/H\text{-beta-}Al_2O_3$ catalyst: effect of zeolite crystal size in the nanoscale range. *Ind. Eng. Chem. Res.* **42,** 2773–2782 (2003).
27. Awala, H. *et al.* Template-free nanosized faujasite-type zeolites. *Nature Mater.* **14,** 447–451 (2015).
28. de Jong, K. P. *et al.* Zeolite Y crystals with trimodal porosity as ideal hydrocracking catalysts. *Angew. Chem. Int. Edn* **49,** 10074–10078 (2010).
29. Van Santen, R. A. Complementary structure sensitive and insensitive catalytic relationships. *Acc. Chem. Res.* **42,** 57–66 (2009).
30. Gommes, C. J. *et al.* Mesoscale characterization of nanoparticles distribution using X-ray scattering. *Angew. Chem. Int. Edn* **54,** 11804–11808 (2015).

Acknowledgements This work has been supported by the NRSC-C and the European Research Council, EU FP7 ERC Advanced Grant no. 338846. (J.Z. and K.P.deJ.), and by the Flemish government via the Methusalem program (J.A.M.). We thank J. D. Meeldijk for assistance with ultramicrotomy and electron microscopy; M. Rigutto (Shell Projects and Technology) for the zeolite–alumina extrudates; R. Oord and J. Ruiz-Martínez for ammonia TPD measurements; and M. De Prins and S. Radhakrishnan for help with the catalytic experiments.

Author Contributions J.Z. synthesized and characterized the samples, and drafted the manuscript. G.V. performed hydrocracking tests. K.P.deJ. and J.A.M. contributed to experimental design, data analysis and manuscript writing.

Author Information Reprints and permissions information is available at www.nature.com/reprints. The authors declare no competing financial interests. Readers are welcome to comment on the online version of the paper. Correspondence and requests for materials should be addressed to J.A.M. (johan.martens@biw.kuleuven.be) or K.P.deJ. (k.p.dejong@uu.nl).

METHODS

Catalyst synthesis. Cylindrical extrudates with length ~8 mm and diameter ~2 mm, containing 50 wt% of mesoporous zeolite Y (Zeolyst CBV 760, Si/Al = 30 at/at) and 50 wt% of γ-alumina, were obtained from Shell Projects and Technology and are designated as Y/A. Extrudates were crushed and sieved to produce particles of 0.2–0.5 mm and, as such, were used as a support for Pt. $Pt(NH_3)_4(NO_3)_2$ (99.995% purity) was purchased from Sigma-Aldrich, and $H_2PtCl_6{\bullet}6H_2O$ (40 wt% Pt) was purchased from Merck.

Introduction of Pt on the zeolite component—Pt-Y/A catalyst. 1.485 g of 0.2–0.5-mm Y/A particles were suspended in 450 ml Milli-Q water at room temperature and stirred for 1 hour, after which the pH of the suspension was 6.4. Aqueous solution (50 ml) containing 29.8 mg of $Pt(NH_3)_4(NO_3)_2$ was added dropwise to the suspension, after which the pH dropped to 5.3. At these conditions, ion exchange of zeolite protons with $Pt(NH_3)_4^{2+}$ was dominant over electrostatic adsorption on alumina, because the latter surface at pH < 9 is positively charged and does not interact strongly with Pt cations[20]. ICP analysis showed that, under these synthesis conditions, ion exchange led to Pt loading of 0.6 wt% (intake 1.0 wt%) with respect to Y/A. After addition of the Pt precursor, the suspension was stirred for another 3 hours, after which the pH dropped to 4.9. The suspension was filtered and washed with Milli-Q water, and dried in air overnight at 120 °C. Dried catalyst was reduced in a flow of H_2 (gas hourly space velocity, GHSV, ~2,580 h^{-1}) for 3 h at 600 °C, using a ramp of 5 °C min^{-1}.

Introduction of Pt on the alumina component—Pt-A/Y catalyst. A suspension containing 1.491 g of 0.2–0.5-mm Y/A extrudates particles in 450 ml Milli-Q water was stirred for 1 hour at room temperature, after which the pH of the suspension was lowered from 6.2 to 2.6 by adding 1 M HCl solution. To achieve the same Pt loading as for Pt-Y/A, we added 50 ml of aqueous solution containing 22.5 mg of $H_2PtCl_6{\cdot}6H_2O$ salt (pH = 2.7) dropwise to the suspension. At the applied pH range, it is expected that $PtCl_6^{2-}$ will be adsorbed onto the positively charged alumina surface[21], whereas no ion exchange or electrostatic adsorption on the zeolite will take place. ICP analysis confirmed that electrostatic adsorption was complete and that Pt loading was 0.7 wt% (intake 0.6 wt%) with respect to Y/A. After 3 hours of stirring (pH increased to 3.3), the suspension was filtered and washed with Milli-Q water, and dried in air overnight at 120 °C. Dried catalyst was reduced in a flow of H_2 (GHSV ~2,580 h^{-1}) for 3 hours at 600 °C, with a heating ramp of 5 °C min^{-1}, and then heat treated for 1 hour at 600 °C in a flow of 1 vol% O_2 in N_2 (GHSV ~2,580 h^{-1}).

When preparing smaller amounts of catalysts, we decreased the volume of Milli-Q water in the suspension proportionally, while a GHSV of ~3,300 h^{-1} was used for heat treatments; however, we observed no impact of these changes on catalyst structure.

Catalyst characterization. N_2 physisorption measurements were performed on a Micromeritics TriStar 3000 at liquid nitrogen temperature. The sample was dried for 14 h at 300 °C in N_2 flow before measurement.

Temperature-programmed desorption (TPD) of ammonia was performed on a Micromeritics AutoChem II equipped with a thermal conductivity detector (TCD). Before TPD, 0.1 g of catalyst was dried in He for 1 hour at 600 °C, with a heating ramp of 10 °C min^{-1}. The temperature was then decreased to 100 °C and ammonia (10 vol% in He) was adsorbed in a pulse-wise manner until oversaturated, after which the physisorbed ammonia was removed by flowing He for 1 h at 100 °C. The ammonia desorption was monitored until 600 °C with a ramp of 5 °C min^{-1}.

ICP analysis of Pt was performed at Kolbe Mikroanalytisches Laboratorium using an ICP-optical emission spectrometer (Perkin Elmer) after sample dissolution according to standard in-house procedures.

Electron microscopy studies. HAADF imaging and EDX analysis (Figs 2 and 3, Extended Data Fig. 2) were performed on a Talos™ F200X transmission electron microscope (from FEI), equipped with a high-brightness field emission gun (X-FEG) and a Super-X G2 EDX detector. For these analyses, catalysts were embedded in Epofix resin, left to cure in air overnight at 60 °C, and cut to 70-nm sections using a Reichert-Jung Ultracut E ultramicrotome with Diatome Ultra 35° diamond knife. Sections were deposited on carbon-coated copper TEM grids. Images and elemental EDX maps were acquired using Velox™ analytical and imaging software in a scanning transmission mode, with a camera length of 77 mm. Elemental EDX maps of 700 × 700 pixels (Fig. 2) were acquired with a 30-min acquisition time. Elemental EDX maps of 512 × 512 pixels (Fig. 3b, d and Extended Data Fig. 2) were acquired with a 15-min acquisition time and processed in Velox™ using the box filter (3 × 3). Electron tomography was performed using Tecnai 20 (Extended Data Fig. 3a) and Talos™ F200X (Extended Data Fig. 3b) transmission electron microscopes. For electron tomography, catalysts were ground, sonicated in ethanol and drop-casted on Quantifoil R2/1 Cu TEM grids, with a thin carbon film and 5-nm Au particles as fiducial markers. Series of bright-field TEM images were taken with either a bottom-mounted charge-coupled-device camera from TVIPS (Extended Data Fig. 3a) or a Ceta 16 M camera (Extended Data Fig. 3b), over an angle range of ±76° with a tilt increment of 2°. Tilt series were aligned using the IMOD software package[31] and by tracking 5-nm Au fiducial markers from the TEM grid. Aligned series were binned by a factor of 2 and reconstructed in IMOD[31] using the weighted back projection (WBP) algorithm. Resulting reconstructions had a voxel size of $(0.36\,nm)^3$, $(0.34\,nm)^3$, $(0.28\,nm)^3$ or $(0.26\,nm)^3$, depending on the magnification used.

Catalytic tests. Catalytic tests were performed in continuous-flow fixed-bed reactors. *n*-Decane (Sigma) hydroconversion was performed in a high-throughput reactor[32,33]. The catalyst weight was 50 mg; the total pressure was 0.45 MPa; the molar ratio of H_2 to *n*-decane was 214; and the space time at the reactor entrance, *W*/*F* (contact time/rate of gas circulation), was 1,400 kg s mol^{-1}. *n*-Nonadecane (Sigma, 98%) was dissolved in heptane (Acros Organics) at 1 mol% concentration. The mixture was vaporized at 280 °C and mixed with hydrogen before feeding it to the reactor. The catalyst weight was 200 mg; the reaction was performed at a pressure of 0.65 MPa; the molar ratio of H_2 to hydrocarbons was 14.6; and *W*/*F* was 713 kg s mol^{-1}. Under the investigated reaction conditions, heptane was confirmed to be inert. The same reaction conditions as for *n*-nonadecane conversion were used for pristane (Sigma, 98%) hydroconversion. The reaction products were analysed by on-line gas chromatography over an apolar capillary column (HP-1) and flame ionization detector. In both reactors, temperature was increased stepwise, and the reaction was equilibrated for 1 hour before product sampling.

31. Kremer, J. R., Mastronarde, D. N. & McIntosh, J. R. Computer visualization of three-dimensional image data using IMOD. *J. Struct. Biol.* **116,** 71–76 (1996).
32. Huybrechts, W., Mijoin, J., Jacobs, P. A. & Martens, J. A. Development of a fixed-bed continuous-flow high-throughput reactor for long-chain n-alkane hydroconversion. *Appl. Catal. A* **243,** 1–13 (2003).
33. Burnens, G., Bouchy, C., Guillon, E. & Martens, J. Hydrocracking reaction pathways of 2,6,10,14-tetramethylpentadecane model molecule on bifunctional silica–alumina and ultrastable Y zeolite catalysts. *J. Catal.* **282,** 145–154 (2011).

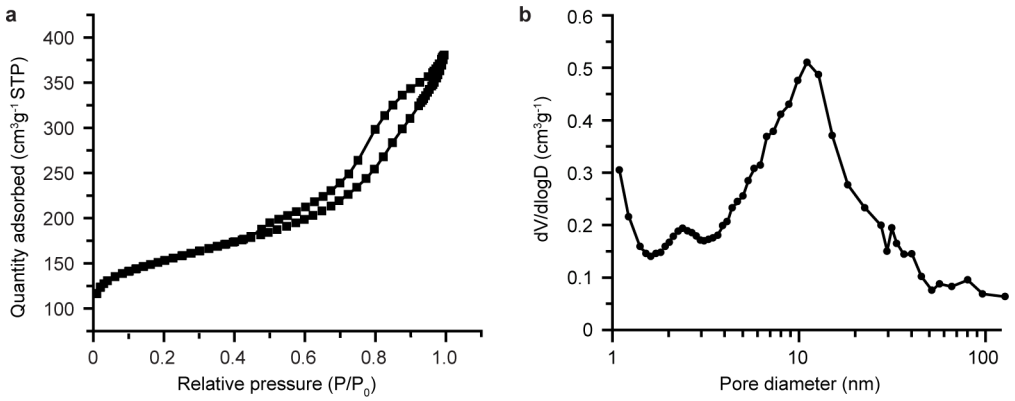

Extended Data Figure 1 | Textural analysis of Y/A extrudates. **a**, N_2 physisorption isotherm (adsorption and desorption), plotting the adsorbed N_2 volume (in $cm^3\ g^{-1}$), referred to a standard temperature and pressure (STP) of 0 °C and 1 atmosphere, against the relative pressure, P/P_0. The isotherm shows the hysteresis loop that is indicative of the presence of mesopores (of diameter 2–50 nm). In addition, the quantity of N_2 that is adsorbed at very low relative pressure indicates the presence of micropores (of diameter ~1 nm). **b**, The Barrett–Joyner–Halenda (BJH) pore-size distribution, derived from the adsorption branch of the isotherm in **a**, points to the broad size distribution of mesopores and macropores (macropores having a diameter greater than 50 nm). V is the pore volume; D is the pore diameter.

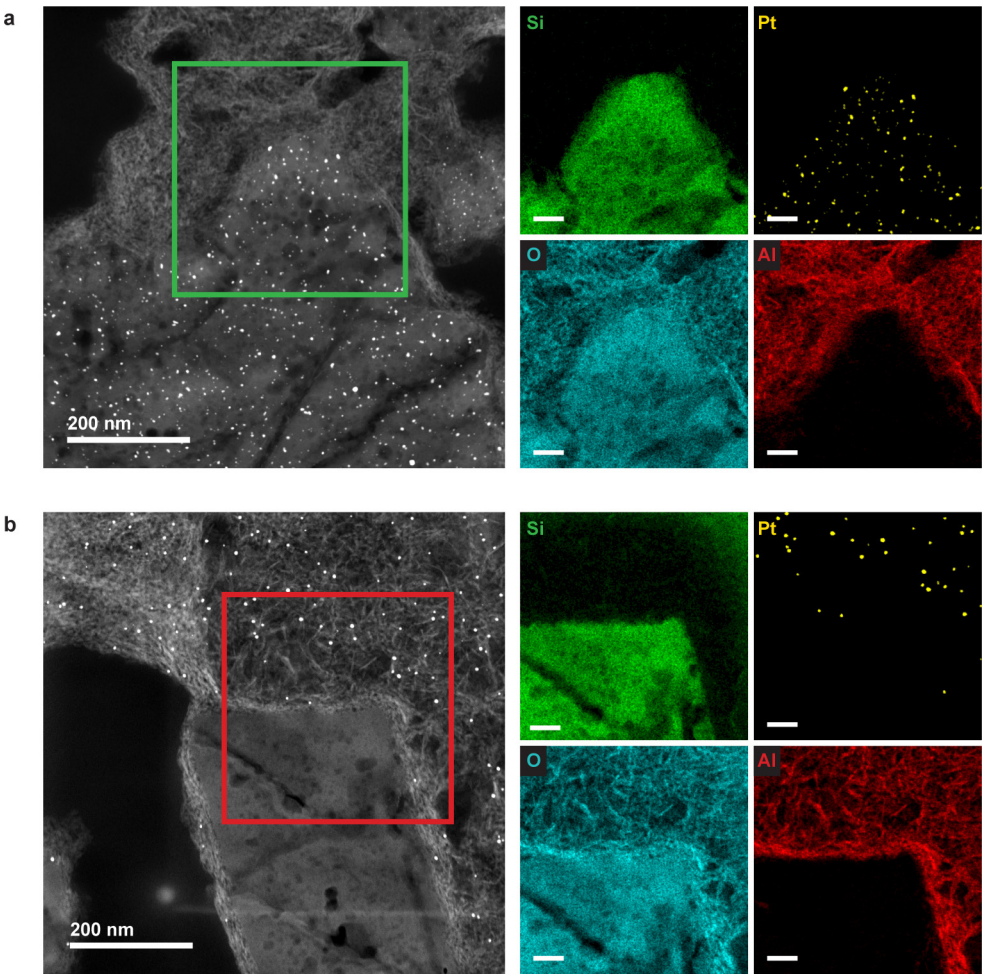

Extended Data Figure 2 | Controlled deposition of platinum. a, Left, an HAADF-STEM image of a 70-nm-thick section of the Pt-Y/A catalyst. Right, EDX elemental maps of the region outlined in green in the HAADF-STEM image. The EDX maps show the presence of Pt particles (yellow) in the zeolite region (green, with the dominant Si signal); the alumina region (red) is empty. 'O' denotes the oxygen signal. **b**, Left, an HAADF-STEM image of a 70-nm-thick section of the Pt-A/Y catalyst. Right, EDX elemental maps of the region outlined in red at the left. Pt particles (yellow) are present in the alumina region (red), while the zeolite crystal (green) contains no Pt particles. The bright spot and line in the HAADF-STEM image of Pt-A/Y, below the mapped region of interest, originate from prolonged electron-beam exposure. Scale bars in the EDX maps represent 50 nm.

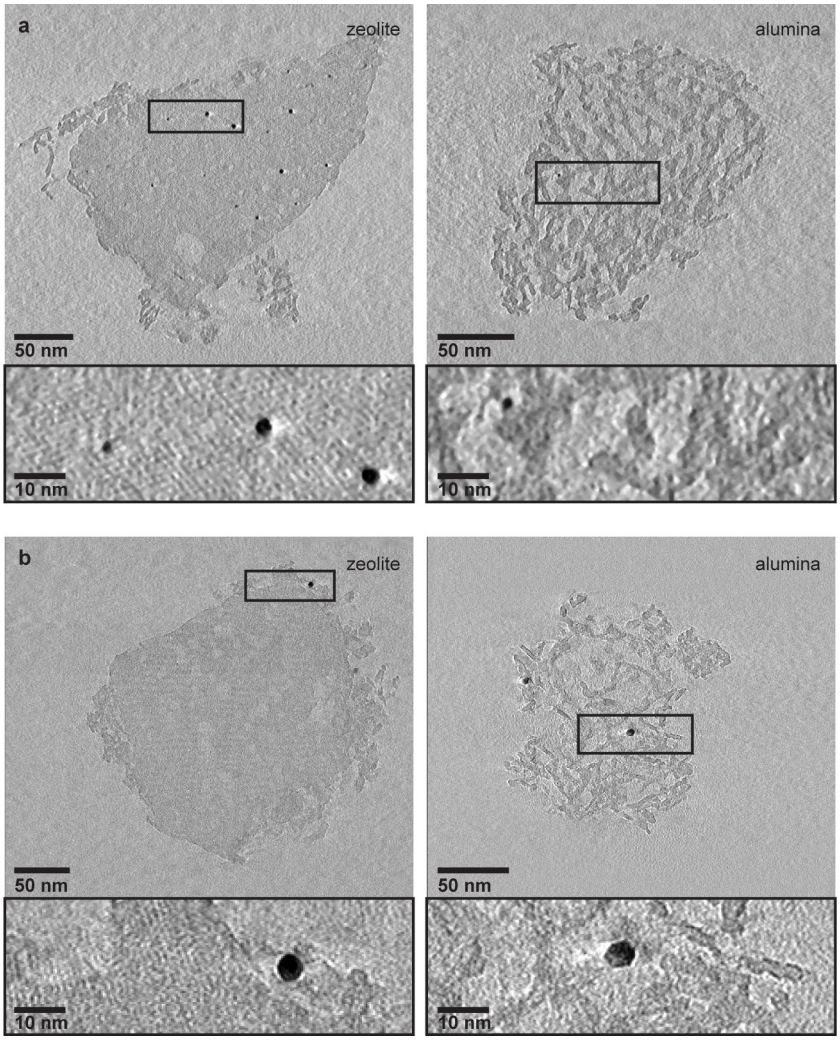

Extended Data Figure 3 | Three-dimensional structural analysis using electron tomography. a, Pt-Y/A catalyst. One-pixel slices, equal to thicknesses of 0.34 nm (left) and 0.26 nm (right), from the middle of the electron-tomography reconstructions of zeolite crystal (left) and alumina aggregate (right) from the Pt-Y/A catalyst, show the presence of ~2.5-nm Pt particles inside the zeolite crystal (left). Within the alumina aggregate (right), only a very few Pt particles were detected, of which one is shown in the zoomed-in region. **b**, Pt-A/Y catalyst. Ten-pixel slices, equal to thicknesses of 3.6 nm (left) and 2.8 nm (right), from the middle of the electron-tomography reconstructions of zeolite crystal (left) and alumina aggregate (right) from the Pt-A/Y catalyst, show that Pt particles of ~3.5-nm diameter were located on the alumina platelets surrounding the zeolite crystal (left) and on the alumina platelets of the aggregate (right). No Pt particles were detected inside the zeolite crystal. For electron-tomography analysis, both catalysts were ground, dispersed in ethanol, and sonicated in order to break zeolite crystals and alumina aggregates apart and analyse them separately on the TEM grid.

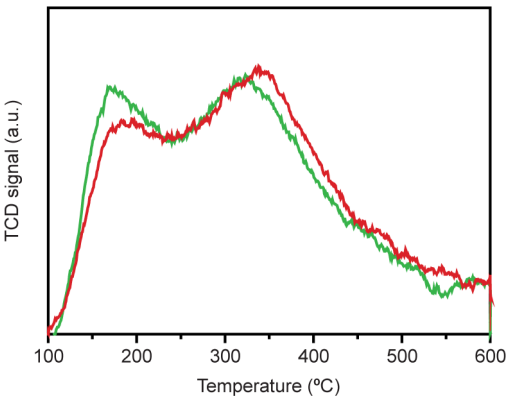

Extended Data Figure 4 | Comparing the acidity of the samples. Temperature-programmed desorption of ammonia by the Pt-Y/A (green) and Pt-A/Y (red) catalysts displays peaks that indicate the presence of weakly acidic (at ~160 °C) and strongly acidic (at ~320 °C) sites within both catalysts, with Pt-A/Y showing slightly lower peak intensity in the region of the weakly acidic site. The total amount of ammonia desorbed was measured to be 14.3 $cm^3 g^{-1}$ (Pt-Y/A) and 14.7 $cm^3 g^{-1}$ (Pt-A/Y) STP.

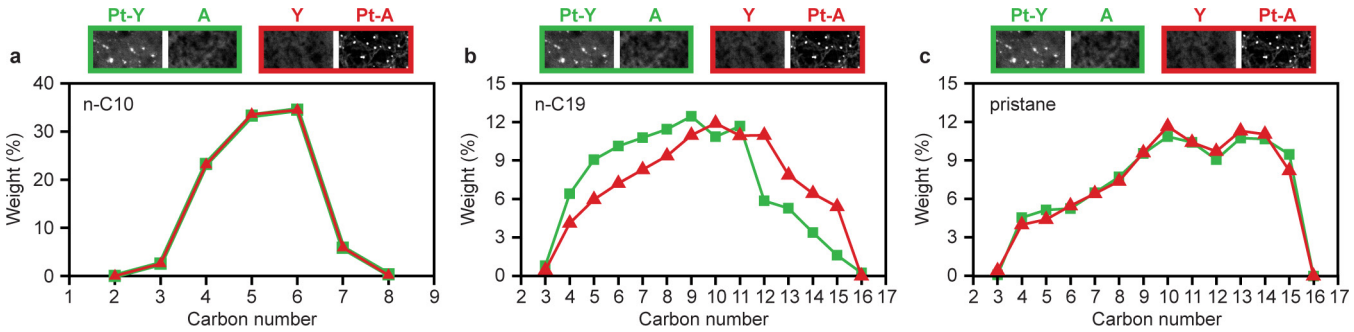

Extended Data Figure 5 | Hydrocracking product distribution at 35% cracking conversion. a, *n*-Decane feed; **b**, *n*-nonadecane feed; **c**, pristane feed. Results obtained with Pt-Y/A and Pt-A/Y catalysts are represented with green squares and red triangles, respectively. Experiments were performed at a pressure of 0.45 MPa and H_2/hydrocarbon molar ratio of 214 (*n*-decane); or a pressure of 0.65 MPa and a H_2/hydrocarbon molar ratio of 14.6 (*n*-nonadecane and pristane).